ACS SENSORS

pubs.acs.org/acssensors

Article

Attomolar Sensitivity in Single Biomarker Counting upon Aqueous Two-Phase Surface Enrichment

Zi Li, Molly McNeely, Erin Sandford, Muneesh Tewari,* Alexander Johnson-Buck,* and Nils G. Walter*

Cite This: *ACS Sens.* 2022, 7, 1419−1430

Read Online

ACCESS | Metrics & More | Article Recommendations | Supporting Information

ABSTRACT: From longstanding techniques like enzyme-linked immunosorbent assay (ELISA) to modern next-generation sequencing, many of the most sensitive and specific biomarker detection assays require capture of the analyte at a surface. While surface-based assays provide advantages, including the ability to reduce background by washing away excess reagents and/or increase specificity through analyte-specific capture probes, the limited efficiency of capture from dilute solution often restricts assay sensitivity to the femtomolar-to-nanomolar range. Although assays for many nucleic acid analytes can decrease limits of detection (LODs) to the subfemtomolar range using polymerase chain reaction, such amplification may introduce biases, errors, and an increased risk of sample cross-contamination. Furthermore, many analytes cannot be amplified easily, including short nucleic acid fragments, epigenetic modifications, and proteins. To address the challenge of achieving subfemtomolar LODs in surface-based assays without amplification, we exploit an aqueous two-phase system (ATPS) to concentrate target molecules in a smaller-volume phase near the assay surface, thus increasing capture efficiency compared to passive diffusion from the original solution. We demonstrate the utility of ATPS-enhanced capture via single molecule recognition through equilibrium Poisson sampling (SiMREPS), a microscopy technique previously shown to possess >99.9999% detection specificity for DNA mutations but an LOD of only ∼1−5 fM. By combining ATPS-enhanced capture with a Förster resonance energy transfer (FRET)-based probe design for rapid data acquisition over many fields of view, we improve the LOD ∼ 300-fold to <10 aM for an *EGFR* exon 19 deletion mutation. We further validate this ATPS-assisted FRET-SiMREPS assay by detecting endogenous exon 19 deletion molecules in cancer patient blood plasma.

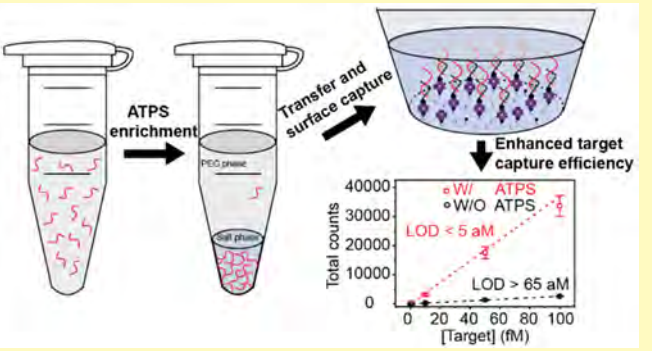

KEYWORDS: *aqueous two-phase system, target enrichment, ultrasensitive detection, single-molecule fluorescence microscopy, Förster resonance energy transfer, kinetic fingerprinting*

A wide range of surface-based assays including microarrays,[1,2] enzyme-linked immunosorbent assay (ELISA),[3] optical/electrochemical biosensors,[4] and modern next-generation sequencing methods[5] require the analytes to travel to a solid substrate for subsequent detection or sequencing. The mass transport of analytes from solution to the surface plays a critical role in governing the capture efficiency and the limit of detection of assays, which ultimately constrains their analytical performance. For example, since the single-molecule real-time sequencing platform by Pacific Biosciences utilizes nanoscale zero mode waveguides (ZMW) to capture the polymerase-bound DNA complexes for sequencing, the capture efficiency, defined as the number of ZMW occupied by the complexes over the total number of ZMW, controls the throughput of the sequencing results.[6] Although adding more starting materials can improve the capture efficiency of the analyte complexes by ZMW, it will also increase the cost. As another example, in the case of DNA microarrays,[1] the hybridization efficiency of target DNA molecules to complementary probe DNA immobilized on the surface can be limited by the slow diffusion of the target DNAs to the surfaces, resulting in long hybridization times and low throughput. This phenomenon of diffusion-limited capture and detection is even more problematic in highly dilute samples, such as blood samples from cancer patients containing very low concentrations of circulating tumor DNA (ctDNA).[7] Therefore, mass transport-limited assay performance is a ubiquitous challenge that needs to be addressed and solved to advance a multitude of surface-based analytical technologies.

To improve the capture efficiency and/or detection sensitivity of surface-based assays, a variety of methods have been proposed and applied, including the application of

Received: January 17, 2022
Accepted: April 6, 2022
Published: April 19, 2022

polymerase chain reaction (PCR) to amplify the target of interest,[8] microfluidics-assisted enrichment,[9,10] and external forces such as electric or magnetic fields for the preconcentration of target.[11] For nucleic acid targets, PCR amplification is by far the most popular approach to increase sensitivity; however, amplification steps can introduce bias and errors, resulting in false positives or negatives.[12] Additionally, heat-induced chemical damage generated during amplification can yield new mutations that present as false positives in some assays.[13,14] Furthermore, PCR-based assays are vulnerable to environmental cross-contamination when the same or similar PCR products have been previously handled in the same space, and are easily introduced or carried over through DNA-containing aerosols generated during amplification setup or product handling, leading to false-positive results.[15] Finally, many analytes, such as short nucleic acid fragments, epigenetic modifications, and proteins, cannot be amplified efficiently or at all.

Because of these caveats, there is strong motivation to seek direct, amplification-free detection approaches. However, the detection sensitivity of amplification-free assays is low compared to PCR-based approaches, limited largely by the slow mass transport of analytes and finite affinity of surface capture. For example, state-of-the-art surface-based or bead-based nucleic acid assays have limits of detection (LODs) of 0.1−10 fM.[16] Incorporation of microfluidics in assay design has offered a means to improve the mass transport of analytes to some degree. For instance, Nguyen et al.[10] developed microfluidics-assisted fluorescence *in situ* hybridization (FISH) with the application of square-wave oscillatory flows of diluted probe solutions in a thin microfluidic chamber of 5 μL volume, which reduces hybridization time of FISH probes to target DNA strands from overnight to 4 h and decreases the consumption of the expensive probe solutions by a factor of 5. Martins et al.[17] utilized an ion concentration polarization-based microfluidic concentrator to accelerate the mass transport of DNAs onto microarrays by concentrating a ∼microliter fluidic DNA sample into a ∼nanoliter plug located near DNA probe-immobilized surfaces and reported a maximally achievable detection sensitivity of ∼1 nM for the model morpholino microarray. However, the design and implementation of microfluidics to hybridization-based assays is sophisticated and time-consuming, with only a limited sensitivity improvement, insufficient for many applications.

Aqueous two-phase systems (ATPSs) have been applied to the extraction, purification, and enrichment of biomolecules including proteins, nucleic acids, plasmid DNAs, and cells.[18] A typical ATPS comprises two water-soluble polymers, or a polymer and a salt, that form two immiscible aqueous phases upon the introduction of water. Compared to the two-polymer system, polymer−salt ATPSs have some key advantages. First, polymer−salt systems generally cost less than two-polymer systems such as the poly(ethylene glycol) (PEG)-dextran system. Second, the denser, salt-rich phase of a polymer−salt system generally has a lower viscosity than two immiscible polymer phases, facilitating liquid handling and, importantly for the present study, faster diffusion of dissolved analyte.[19] In a polymer−salt ATPS, PEG is often used as the polymer. Among different salt options, citrate is considered to be more environmentally friendly and less toxic due to its biodegradability. The PEG-citrate ATPS has also proven to be useful for purifying antibodies[20] and plasmid DNA,[21] where specific biomolecules largely partition into one phase or the other for recovery at higher purity. Previously, a PEG-dextran ATPS was used in multiplex ELISA assays for cross-reaction-free detection of multiple antigens, since detection antibodies partition into the denser dextran phase and are retained there without diffusive dispersion.[22] In this work, we demonstrate that ATPS can also be used to enhance the surface capture of nucleic acid analytes in a surface-based assay, resulting in substantially higher analytical sensitivity.

We previously developed an ultraspecific and amplification-free detection method termed single-molecule recognition through equilibrium Poisson sampling or SiMREPS to detect miRNAs,[23] DNAs,[14] and protein targets[24] with low femtomolar sensitivity. SiMREPS utilizes the transient and reversible binding of fluorophore-labeled detection probes to surface-captured targets to generate kinetic patterns or fingerprints for distinguishing nonspecific probe binding from binding to the target.[25,26] A specificity of 99.99999% for detecting point mutations was demonstrated using SiMREPS, permitting the detection of one mutant DNA molecule in a background of more than one million wild-type DNA molecules.[14] However, even though SiMREPS can achieve extremely (in principle, arbitrarily) high specificities, the sensitivity of SiMREPS assays with diffusion-limited surface capture is not yet sufficient to detect low-abundance targets such as ctDNA in biofluids. This is due to a combination of low capture efficiency of the analyte from bulk solution and the typically long (2 to 10 min) acquisition time per field of view (FOV), resulting in the detection of only a tiny fraction of the available analyte.[24]

In this study, we used SiMREPS as a model analytical technique to illustrate the power of ATPS in increasing target capture efficiency by enriching a target ctDNA into a small sample volume, thus facilitating its mass transport to the assay surface for ∼20-fold higher sensitivity. We further incorporated single-molecule Förster resonance energy transfer (smFRET) to increase the imaging efficiency (number of FOVs imaged per sample well) of SiMREPS assays, reducing the acquisition time per FOV by a factor of 20 and permitted the rapid imaging of a much larger fraction of surface-captured target molecules. The combination of ATPS and smFRET yields limits of detection (LODs) of <10 aM for EGFR exon 19 deletion mutant DNA, or a total increase of approximately 300-fold in sensitivity compared to previously reported SiMREPS assays. The ATPS-assisted, FRET-based SiMREPS assay was further validated by detecting the endogenous EGFR exon 19 deletion mutation in cancer patient blood plasma as a proof-of-concept for the direct quantification of rare ctDNA molecules from human plasma.

EXPERIMENTAL SECTION

Chemicals and Materials. Poly(ethylene glycol) (PEG) with an average molecular weight of 3350 Da, sodium citrate dihydrate, and (3-aminopropyl)triethoxysilane were purchased from Sigma-Aldrich (catalog no. P4338-500G, W302600-1KG-K, A3638-100 ML, respectively). Sodium chloride was purchased from Fisher (catalog no. S271-10). Biotin-PEG-SVA and mPEG-SVA were obtained from Laysan Bio, Inc. (catalog no. BIO-PEG-SVA-5K-100MG and MPEG-SVA-5K-1g, respectively). Disulfosuccinimidyltartrate was purchased from Soltec Ventures Inc. (catalog no. CL107). Sodium bicarbonate was purchased from Acros Organics (catalog no. AC217120010). All chemicals were used without further modification or purification.

Oligonucleotides. All the DNA oligonucleotides used in this study were purchased from Integrated DNA Technologies (IDT) with either standard desalting purification or, in the case of fluorophore-labeled oligonucleotides, high-performance liquid chromatography

https://doi.org/10.1021/acssensors.2c00135
ACS Sens. 2022, 7, 1419−1430

(HPLC) purification. Capture probes with biotin and locked nucleic acid modifications were purchased from Exiqon with HPLC purification. All oligonucleotide sequences are shown in Table S1. To detect exon 19 deletion mutations (COSMIC ID: COSM6223; COSM6225), a Cy5-labeled fluorescent probe was specifically designed for each mutation, and an additional Cy3-labeled fluorescent probe was used as a FRET donor in both assays. Double-stranded DNA (dsDNA) targets with 160 base pairs in length were obtained by mixing complementary oligonucleotides (1 μM each strand) in annealing buffer (10 mM Tris−HCl [pH 8.0 at 25 °C], 50 mM NaCl, 1 mM ethylenediaminetetraacetic acid (EDTA)), heating at 95 °C for 3 min, and then slowly cooling to 25 °C for 25 min. All the oligonucleotides were aliquoted and stored at −20 °C prior to use. Healthy plasma cell-free DNA (cfDNA) was extracted from blood collected from healthy people.

Plasma Collection and cfDNA Isolation. Human blood samples were collected with informed consent under University of Michigan Institutional Review Board protocol HUM00092161. Peripheral blood samples were collected in EDTA-containing tubes for the healthy control samples and in a Streck Cell-Free DNA BCT for the lung cancer patient with the exon 19 deletion. Blood samples were transported to the lab at room temperature and processed through a double centrifugation technique. The plasma was first centrifuged at 1600*g* for 10 min at room temperature. The top plasma layer was transferred to microcentrifuge tubes and centrifuged at 16,000*g* for 10 min at room temperature. Plasma above the remaining pellet was then aliquoted into fresh microcentrifuge tubes and frozen at −80 °C until DNA extraction.

Plasma samples were thawed at room temperature prior to cfDNA extraction. Healthy control plasma samples from 6 different control subjects were pooled prior to cfDNA extraction. Plasma cfDNA was extracted using the QIAamp Circulating Nucleic Acid Kit (Qiagen), following the manufacturer's guidelines with the following modifications: (1) carrier RNA was not added to the ACL Lysis buffer; (2) for the plasma collected in the Streck Cell-Free DNA BCT, the incubation period during the 60 °C heat treatment was 60 min.[27] Extracted cfDNA was quantified using the Qubit dsDNA High Sensitivity Assay Kit (Invitrogen), following the manufacturer's protocol. 838.1 ng of cfDNA (representing 85.5 mL of plasma) was contained within the healthy control extract and 23.04 ng of cfDNA (representing 0.4 mL of plasma) was contained within the exon 19 deletion subject extract.

Preparation of the Aqueous Two-Phase System. The ATPS used in this study was composed of PEG 3350, sodium citrate dihydrate, and sodium chloride. To prepare the ATPS, a master mix was prepared by dissolving 6.56 g of PEG 3350, 0.348 g of sodium citrate dihydrate, and 0.498 g of sodium chloride in 30 mL of milli-Q purified water in a 50 mL centrifuge tube. The mixture was well mixed by vortexing at high speed until the powder was fully dissolved. Then, the aqueous solution was centrifuged at 1000*g* for 1 min under ambient temperature to remove air bubbles. Small volumes (36 or 216 μL) of ATPS master mix solution were aliquoted into GeneMate 2 mL low-adhesion microcentrifuge tubes (VWR, catalog no. 490003-302), flash-frozen with liquid nitrogen, and lyophilized. The ATPS aliquots were stored at room temperature. The amount of powder obtained from 36 μL of master mix solution (referred to as "0.1× ATPS") was used to dissolve 10 μL sample solutions, while 216 μL of the master mix solution gave sufficient ATPS after lyophilization (referred to as "0.6× ATPS") to dissolve 60 μL sample solutions for assay preparation. The final composition of the ATPS after sample addition in each case was 37.7% (w/w) PEG 3350, 2% (w/w) sodium citrate, and 2.8% (w/w) sodium chloride.

Preparation of ATPS-Assisted, FRET-Based SiMREPS Assay. In contrast to previously published SiMREPS assays,[14,23] here we applied two additional strategies: ATPS to preconcentrate target molecules for higher sensitivity, and smFRET to reduce the data acquisition time per field of view by improving the signal-to-noise ratio (S/N) at high probe concentrations (>100 nM). To facilitate preconcentration of a small volume onto a specific region of the assay surface, a 3D-printed strip well with openings 1.2 mm or 2 mm in diameter was designed and used for the ATPS-based SiMREPS assay. The 3D-printed strip wells were designed in Fusion 360 (Autodesk) and 3D-printed with a z-feature resolution of 16 μm from VisiJet m3 crystal material using a Projet 3500 3D printer at the Duderstadt Center's Fabrication Studio at University of Michigan. 3D-printed well strips were cleaned of support resin by sonicating in warm water (45−50 °C) multiple times until the washing water was almost clear. The washed 3D-printed wells strips were rinsed thoroughly with absolute ethanol (200 proof; Thermo Fisher, catalog no. T038181000) and then rinsed again with distilled water. Finally, the wells were blown dry using nitrogen. The 3D-printed strip well (5 wells in a row) was attached to biotin-PEG functionalized coverslips (prepared as described in our previously published papers[14,25]) with a fast-curing Epoxy adhesive (Ellsworth adhesives, hardman double, catalog no. 4001), using an electronics vise equipped with double-sided tape to carefully lower the well strip onto each coverslip with minimal lateral movement, which might damage the biotin-PEG coating. The 1.2 mm-diameter sample well creates a surface area of 1.13 mm^2, which can be covered by the salt phase of ATPS with addition of 10 μL of sample solution, while the 2 mm-diameter sample well gives a surface area of 3.14 mm^2 that can be filled with the salt phase generated by 0.6× ATPS phase separating 60 μL of the sample solution.

At the start of an assay, each well was washed once with a solution containing 0.05% Tween 20 in T50 buffer and then twice with T50 buffer (10 mM Tris−HCl [pH 8.0 at 25 °C, 50 mM NaCl]. Next, 10 or 20 μL (for 1.2 mm or 2 mm diameter 3D-printed samples wells) of 1 mg/mL of streptavidin was added into the sample wells and incubated for 10 min to allow streptavidin to bind to the biotin-PEG on the coverslip surface. Wells were then washed three times with 100 μL of 1× phosphate buffered saline (PBS) buffer to remove excess streptavidin, followed by incubation with 10 or 20 μL of 100 nM biotinylated and LNA-modified capture probes for 10 min. Wells were then washed with 1× PBS three times, and the final wash left in the well until sample addition.

To prepare target DNA solutions, we combined the previously annealed target (mutant) dsDNA with 10 nM each of six short DNA oligonucleotides (tiles) complementary to parts of target DNA sequence and 2 μM $(dT)_{30}$ in 1× PBS. The tiles were designed to inhibit rehybridization of the two complementary target DNA strands after melting, providing the target in single-stranded form for the SiMREPS assay, while the $(dT)_{30}$ serves as a carrier to prevent losses of low concentrations of the target DNA to nonspecific adsorption. For spike-in experiments, target DNA solutions also contain wild-type DNA or healthy plasma cfDNA with the presence of wild-type blocker designed to block the potential capturing of wild-type DNA onto the surface during sample incubation. The target solutions were denatured at 95 °C for 2 min in a thermocycler, and then kept at 40 °C for 8 min to permit the short DNA tiles to bind to the target DNA sequence, followed by cooling in a room-temperature water bath for 5 min. The appropriate volume of target DNA solution was then added to an aliquot of lyophilized ATPS prepared previously (10 μL target DNA solution for 0.1× ATPS aliquots, or 60 μL target DNA solution for 0.6× ATPS aliquots), and then vortexed at maximum speed for 2 min, followed by centrifuging at 10,000*g* for 1 min. A custom 3D-printed coverslip holder was used to hold the coverslip in place inside the swinging bucket. A clear droplet at the bottom of the ATPS mixture was formed, indicating successful phase separation. The clear droplet contained the target molecules and other oligonucleotides added during target solution preparation.

The droplet containing concentrated target molecules and the rest of the ATPS were transferred into the sample wells that had been coated with streptavidin and biotinylated capture oligonucleotide, and were centrifuged at 3000 rpm (1439*g*) in a swinging-bucket centrifuge (Eppendorf, Centrifuge 5804 R 15 A version) for 2 h at room temperature. Next, samples were removed from the wells, and the wells were washed once with 4× PBS and twice with 1× PBS. Ten microliters of a 1× PBS solution containing 5 μM capture probe blockers that are fully complementary to the capture probe sequence was introduced into each sample well to block unoccupied capture

https://doi.org/10.1021/acssensors.2c00135
ACS Sens. 2022, 7, 1419−1430

probe sites. Then, 10 μL of a 4× PBS solution containing 100 nM auxiliary probe that provides a docking site on the target molecule for the Cy3-labeled FRET donor probe was added to each well and incubated for 10 min. The auxiliary probe solution was removed and replaced with 1× PBS buffer until the imaging solution was added. Finally, 100 μL of an imaging buffer containing an oxygen scavenger system (50 nM protocatechuate dioxygenase, 1 mM Trolox and 5 mM 3,4-dihydroxybenzoate), 400 nM Cy3-labeled fluorescent probe, and 600 nM Cy5-labeled fluorescent probe was added to each well immediately before imaging.

Single-Molecule Förster Resonance Energy Transfer Microscopy. Single-molecule FRET imaging was performed on an Olympus IX-81 objective-type TIRF microscope equipped with a CellTIRF motorized TIRF illumination module, a 60× oil-immersion objective (APON 60XOTIRF, 1.49 NA), a zt640drc-UF1 dichroic mirror (Chroma), an ET655LP-TRF FRET emission filter (Chroma), a CRISP autofocusing system (Applied Scientific Instrumentation, Inc.), and an Evolve 512 EMCCD (Photometrics) operating at an EM gain of 5. Excitation of the FRET donor Cy3 was provided by a 532 nm green laser (Coherent, OBIS 532-120 LS FP) operating at 70 mW output power (~70 mW exiting the objective) at a calculated TIRF penetration depth of 75 nm, and Cy5 emission was detected with an exposure time per movie frame of 200 ms. The combination of smFRET and TIRF illumination greatly reduces any fluorescent background signal generated by the high concentrations of nontarget-bound fluorescent probes. The large concentration of fluorescence probe in turn accelerates probe binding to the target and/or auxiliary probe, reducing the acquisition time per FOV, which increases the assay surface area that can be imaged in a fixed amount of time and, hence, was expected to further improve the sensitivity of our ATPS-based SiMREPS assay. A total of 25 FOVs and 81 FOVs were collected for each sample within 20 or 60 min for 1.2 and 2 mm-diameter 3D-printed wells, respectively. Each FOV was 14 400 μm^2 in size.

Analysis of SiMREPS Data. A custom MATLAB code, described previously,[25] that can identify and analyze regions of repeated binding and dissociation of fluorescent probes in the same location was used to process the SiMREPS data generated by smFRET microscopy. Briefly, we generated an intensity fluctuation map indicating the average absolute frame-to-frame change in intensity at each pixel, and used it to identify 3 × 3-pixel regions of interest (ROIs) comprising repeated appearance and disappearance of FRET signal due to probe binding to the target DNA. Next, for each frame in the video, we calculated the background-subtracted intensity within each ROI and generated an intensity-versus-time trace. Then, hidden Markov modeling (HMM) was applied to the intensity-versus-time traces to identify the binding and dissociation events within each trace. Based on the idealized HMM traces, several parameters that are important for SiMREPS kinetic fingerprinting analysis were determined including N_{b+d}, the number of binding and dissociation events; $\tau_{bound,\ median}$ and $\tau_{unbound,\ median}$, the median dwell times in the probe-bound and probe-unbound states, respectively; $\tau_{bound,\ max}$ and $\tau_{bound,\ max}$, the maximum dwell time in the probe-bound and probe-unbound state, respectively; r_{trace} and r_{event}, the signal-to-noise ratios for the entire trace and for the single binding event, respectively. Threshold values for each of these parameters were determined to minimize false positives in controls while maximizing true positives in positive controls containing the target DNA. A custom MATLAB code developed in our lab was also used to optimize the thresholds by training with both a positive and a negative data set.[28]

RESULTS AND DISCUSSION

An ATPS Enables Target DNA Enrichment. Since the limited capture efficiencies and thus detection sensitivities of surface-based assays are significantly caused by the slow mass transport of analytes to assay surfaces, preconcentrating or enriching the target molecules into a small volume that is in close proximity of the capture or detection surface is expected to be highly beneficial to assist the mass transport of the analytes. Figure 1 shows a schematic comparison of two conditions: one where analytes passively diffuse to the capture probe-modified surface, and one where an ATPS-assisted capture process is used. The analytes shown in Figure 1 are nucleic acid targets, but they can also be other biomolecules including proteins, enzymes,[29] and antibiotics,[30] provided that an ATPS is available that strongly partitions the analyte into one phase.

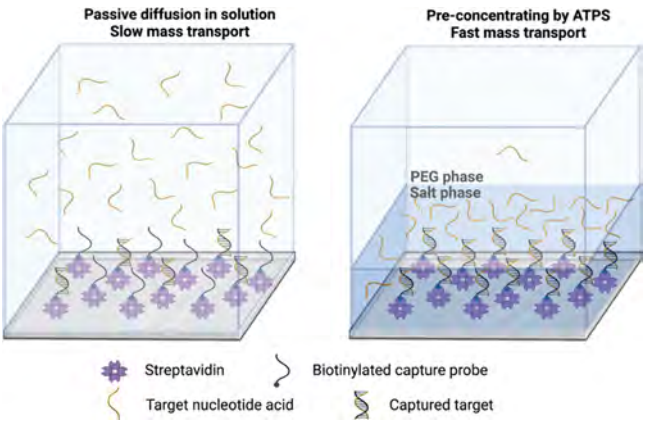

Figure 1. Schematic illustrating the enhancement of mass transport of analytes (nucleic acids, small ligands, or proteins) to capture probe-modified surfaces using an ATPS when compared to passive diffusion of analytes from dilute, homogeneous aqueous solution.

To test the performance of an ATPS in enhancing the mass transport of target molecules for capture on detection surfaces of bioassays, we aimed to improve the sensitivity of a SiMREPS assay of a cancer-related DNA mutation using an ATPS composed of PEG (average molecular weight, MW ~ 3350 Da), sodium citrate, and sodium chloride to enrich the target molecules in a small volume near the assay surface during the capture step. In the PEG-citrate ATPS, a second salt, sodium chloride, is added to enhance the partitioning of nucleic acids into the salt-rich phase.[31] First, to better understand what bulk compositions would promote the formation of an ATPS, a binodal curve with a constant mass of sodium chloride and varying PEG (MW 3350) and sodium citrate was measured using the cloud-point titration method (Supporting Information, Figure S1). The final composition of the ATPS we used (shown as the red star in Figure S1, PEG 37.7%, SC 2% and NaCl 2.8 wt %%) was selected to yield a volume of the salt-rich phase that is just large enough to span the entire detection surface in the sample well, but no larger. To demonstrate phase separation of the selected ATPS, we prepared a 1 μM, Cy3-labeled DNA oligonucleotide (44 nt in length) solution and added 10 and 60 μL of the solution into the corresponding lyophilized ATPS aliquots, termed 0.1× ATPS and 0.6× ATPS, respectively. After vigorous vortexing for 2 min and centrifuging at 10,000g for 1 min, a clear phase separation was observed, wherein the Cy3-labeled DNA oligonucleotides were concentrated from the original light-pink solution into a much smaller, dark-pink salt-rich phase (Figure 2a–c).

Next, we examined the capability of the ATPS to concentrate a target DNA (exon 19 in-frame deletion, COSMIC ID: COSM 6225, single-stranded, 160-nucleotide in length) by UV spectrophotometry. First, a master mix of the selected ATPS was prepared and vigorously mixed to achieve the homogeneous distribution of all components in the

https://doi.org/10.1021/acssensors.2c00135
ACS Sens. 2022, 7, 1419–1430

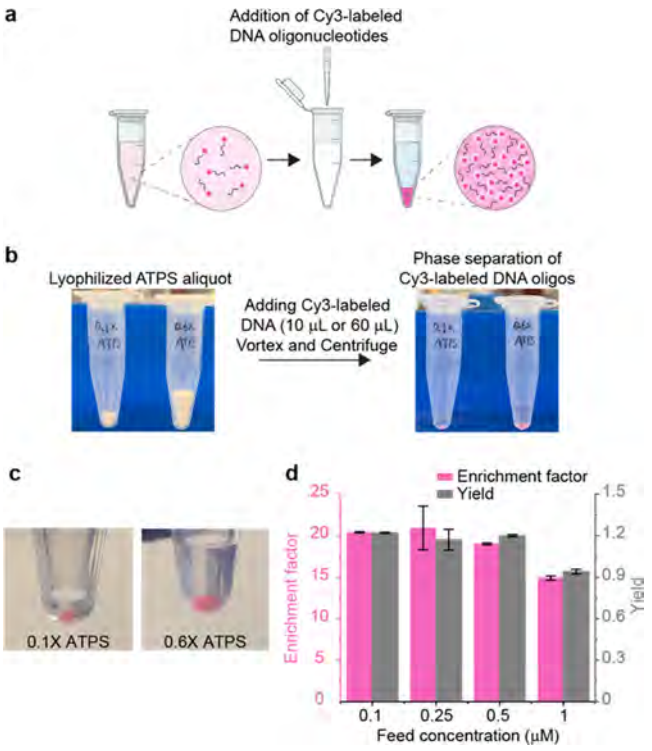

Figure 2. Characterization of partitioning of DNA within the ATPS using a dye-labeled oligonucleotide. (a) A cartoon illustration of the enrichment of dye-labeled DNA oligonucleotides into a small volume after phase separation of the ATPS. (b) Photos illustrating the concentration of a Cy3-labeled oligonucleotide into a smaller salt-rich phase upon adding a dilute solution of the oligonucleotide to lyophilized ATPS aliquots. (c) Zoomed-in views of the salt-rich bottom phase contain the concentrated Cy3-labeled DNA oligonucleotide. (d) Quantitative analysis of the enrichment factor and the yield of a nucleic acid target sequence (*EGFR* exon 19 deletion) after ATPS concentration. The enrichment factor is calculated by dividing the concentration of the nucleic acid in the salt-rich phase by the concentration of the nucleic acid before adding into the ATPS (feed concentration) as determined by UV absorbance. The yield was calculated by dividing the estimated amount of nucleic acid in the salt-rich phase by the amount of feed nucleic acid added into the ATPS. Four sample types with varying input concentrations of the DNA oligonucleotide (0.1, 0.25, 0.5, and 1 μM) were tested. Error bars represent the standard deviation of three independent measurements of the salt phase, wherein a slight overestimation of the small salt-rich phase volume can lead to an apparent yield >1.

mixture. Then, 222.29 mg of the ATPS master mix was weighed into a 2 mL Eppendorf tube using a microscale balance. Subsequently, target DNA solutions of various concentrations (0.1, 0.25, 0.5, and 1 μM) were prepared in a 1× PBS buffer. We added 300 μL of each target DNA solution into individual Eppendorf tubes containing the ATPS mixture. After vortexing and centrifuging, we achieved phase separation with clear phase boundaries. The absorbance of the bottom salt-rich phase containing the enriched target DNA was measured for each sample. As expected, the concentration of each target DNA sample within the salt-rich phase was higher than the original feed concentration since most of the target DNA molecules partitioned into the salt-rich phase, demonstrating the feasibility of applying ATPS for enriching larger DNA fragments that lack fluorescent labels. An enrichment factor was calculated by dividing the preconcentration or feed concentration of the sample by its postconcentration in the salt phase of ATPS. Approximately 20-fold enrichment was achieved for DNA samples with a concentration of 0.1, 0.25, and 0.5 μM (Figure 2d, pink bars). The enrichment factor for the DNA sample with a concentration of 1 μM decreased to about 15-fold, possibly due to less complete partitioning at this highest DNA concentration. We also estimated the yield of the target DNA in the salt phase of the ATPS as the ratio of the amount of target DNA in the salt phase to the amount of target DNA added into the ATPS (Figure 2d, gray bars), further supporting the notion that a 20-fold increase in DNA concentration with a yield close to 1 is achievable as long as the feed concentration is not too high.

ATPS-Mediated Enrichment Improves the Capture Efficiency of Surface-Based Single DNA Molecule Detection. To test the effect of ATPS-mediated target enrichment on surface capture efficiency, we next designed a FRET-based SiMREPS assay for an *EGFR* exon 19 deletion model target (here COSMIC ID: COSM 6223 and COSM 6225) in the form of a synthetic dsDNA with 160 base pairs in length, which we optimized systematically to enhance the detection sensitivity. The 160 bp length of the synthetic dsDNA used in this paper was particularly chosen to represent the short cell-free DNA fragments in biological samples such as blood and urine.[32] A schematic overview of the assay design and workflow is shown in Figure 3. Notably, it features a FRET assay design where the acceptor fluorescent probes are transiently binding to the captured target and the donor fluorescent probes are reversibly binding to the overhang of the auxiliary probes that are tightly bound to the targets. Energy transfer occurs when donor and acceptor fluorescent probes bind to an auxiliary probe-bound target and the same target molecule simultaneously. In addition to adding oligonucleotide dT_{30} as a carrier in high molar excess to reduce losses due to adsorption or reannealing of mutant dsDNA, we found that introducing 10 nM of each of six short oligonucleotides (tiles) that bind the heat-denatured single-stranded target strand significantly improved the sensitivity of the assay for dsDNA (Figure S2). We posit that these tile strands improve surface capture and probe binding by inhibiting dsDNA reannealing and the formation of secondary structure within the target strand. Accordingly, smFRET measurements of surface-captured targets by TIRF microscopy revealed repetitive, proximal binding of the Cy3- and Cy5-labeled fluorescent probe (FPs) to individual surface-captured targets, resulting in single-molecule traces with many transitions between high- and low-FRET signals (Figure 4a,b). These signals can be easily distinguished from less repetitive nonspecific binding signatures that occur in either the presence or absence of a target (Figure 4c), even though the nonspecific signatures may appear as bright in the acceptor channel (Figure 4a). A clear increase in the density of bright fluorescent spots was observed with the application of ATPS for enriching target DNA molecules into a small volume (salt-rich phase) compared to the case without ATPS (Figure S3), indicating that the ATPS improves the capture efficiency as desired. Figure 4c shows a comparison of the accepted counts per FOV for detecting exon 19 deletion COSM 6223 mutant dsDNA with and without the use of the ATPS for target enrichment. The increase in accepted counts per FOV when applying ATPS is approximately 16.5-fold, similar to the 20-fold concentration factors observed in bulk UV absorbance measurements (Figure 2d), demonstrating the ability of an ATPS to enhance the efficiency of target capture and sensitivity of a surface-based assay.

https://doi.org/10.1021/acssensors.2c00135
ACS Sens. 2022, 7, 1419−1430

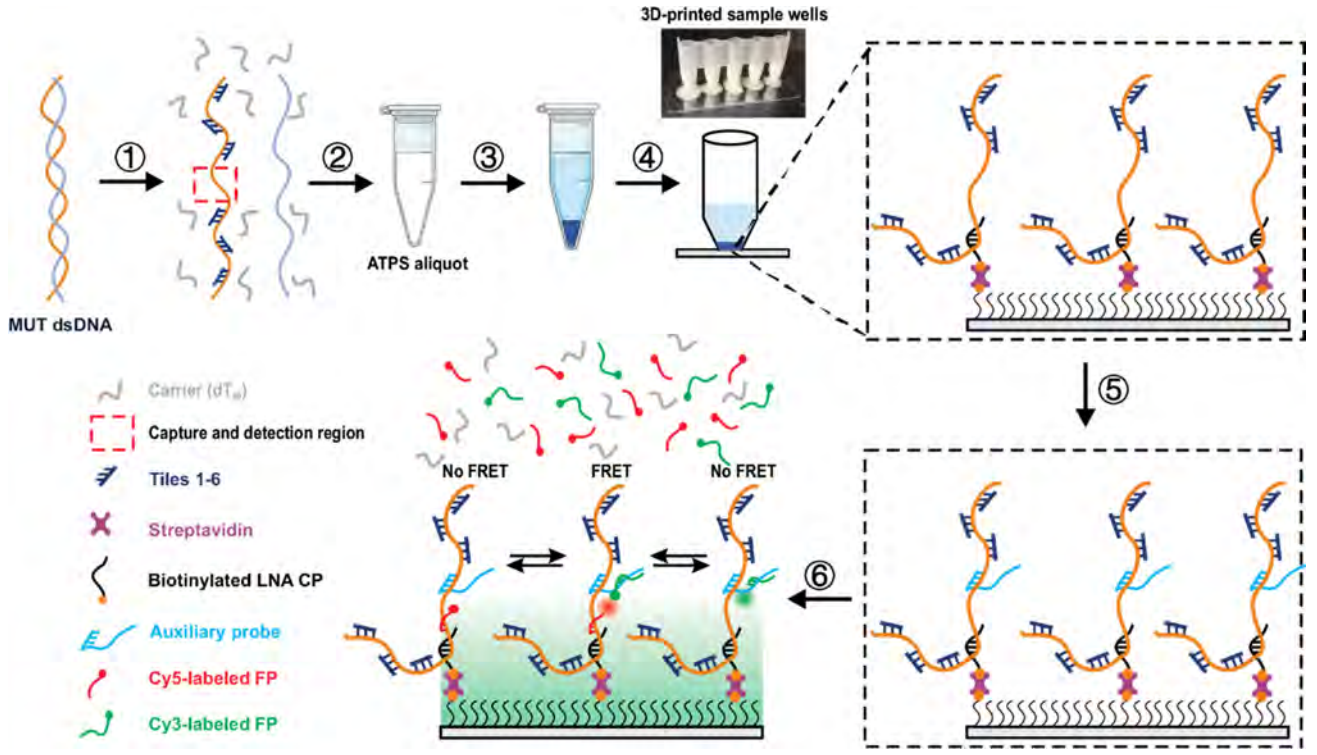

Figure 3. Schematic depicting the sample preparation and measurement steps for an ATPS-enhanced SiMREPS assay. Step 1: Mutant dsDNA is heat denatured; short DNA oligonucleotides 13−18 nucleotides in length ("tiles") subsequently bind to the single-stranded targeted mutant DNA in the presence of a high concentration of single-stranded dT_{30} carrier to prevent the reannealing of complementary target strands and to avoid the formation of secondary structure within the targeted mutant DNA. Step 2: A 10 μL portion of each prepared mutant sample is added into an ATPS aliquot. Step 3: The mixture of target and ATPS is vortexed vigorously for 2 min and then centrifuged at 10,000*g* for 1 min to achieve phase separation. Step 4: The mutant sample in ATPS is transferred to the 3D-printed sample wells attached to a coverslip coated with target gene-specific LNA capture probes. Once successfully transferred, the target mutant DNAs are incubated in the 3D-printed sample wells for 1−2 h to permit surface capture. Step 5: Auxiliary probes are incubated to provide a docking site on the target mutant DNA for the Cy3-labeled FP. Step 6: Single-molecule FRET-SiMREPS (kinetic fingerprinting) using two fluorescent probes (FPs): one labeled with Cy3 (FRET donor) the other labeled with Cy5 (FRET acceptor). The Cy3 FP binds to the auxiliary probe, while the Cy5 FPs binds directly to the site of the captured target DNA bearing the mutation. Since the FRET signal can only be detected when both of the FPs bind simultaneously to the same target complex, a relatively little background signal is observed.

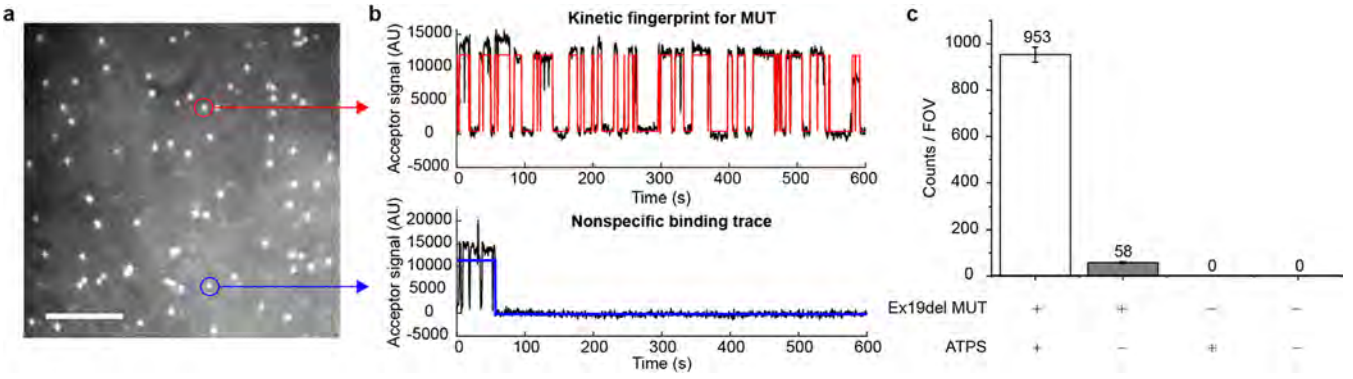

Figure 4. Verification of ATPS-assisted SiMREPS assay performance. (a) Fluorescent image showing FRET signals as bright spots. The image comprises only a small subset of the entire FOV. Scale bar is 3 μm. (b) Representative FRET-SiMREPS traces in the presence of the exon 19 deletion mutant dsDNA target (160 bp) under initial imaging conditions prior to optimization (room temperature, 100 nM FP, 10 min acquisition time), illustrating typical behaviors for traces showing specific target binding kinetics or nonspecific binding. The black line represents the raw FRET signal, while the overlaid red and blue lines represent the idealizations from hidden Markov modeling. (c) Comparison of the number of accepted counts per FOV with and without the application of ATPS from a solution containing an initial target concentration of 100 fM. Error bars represent the standard deviations of the accepted counts from three independent FOVs in each sample.

Accelerated Data Acquisition through Optimized Conditions for FRET-SiMREPS. A main motivation for using FRET-based (Figure 3) detection is that the dependence of the acceptor signal on close proximity of a donor leads to a reduction of background fluorescence and permits the use of much higher FP concentrations (e.g., ~500 nM) than non-FRET detection (~50 nM). The resulting increase in the rate of FP binding to the target potentially is expected to permit

https://doi.org/10.1021/acssensors.2c00135
ACS Sens. 2022, 7, 1419−1430

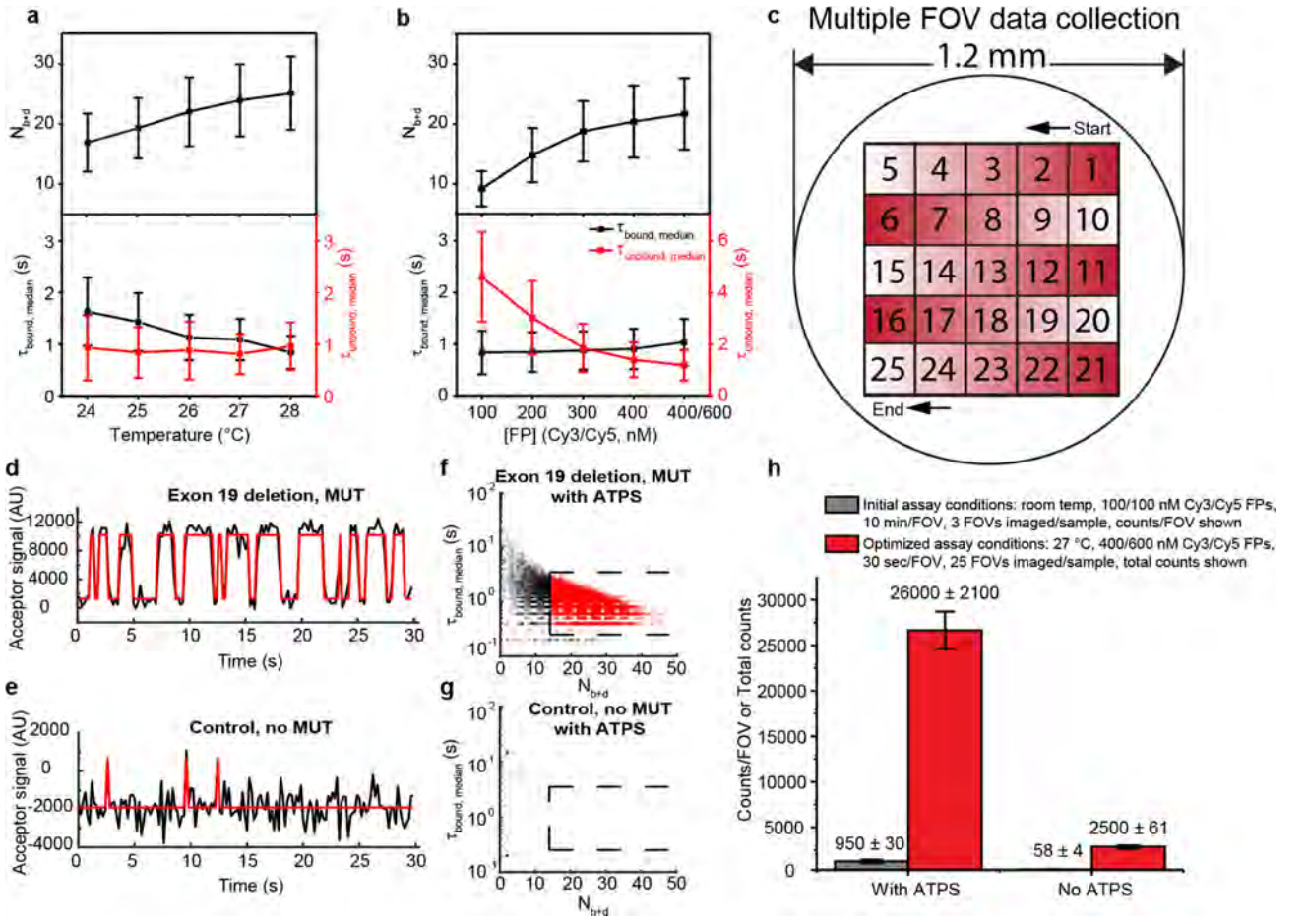

Figure 5. Optimization of detection conditions for rapid imaging to facilitate multiple-FOV data collection. (a) Effect of imaging temperature on the number of binding and dissociation events, as well as the median bound and unbound dwell times, in a 30-s movie. Data points represent the average values of the parameters for 100−1200 traces. The error bars represent one standard deviation across all the accepted traces analyzed under each condition. The concentrations of the Cy3 and Cy5 FP used in the imaging buffer were 400 and 600 nM, respectively. (b) Effect of FP concentration on the number of binding and dissociation events and the median bound and unbound dwell times in a 30 s movie at an imaging temperature of 27 °C. Data points represent the average values of the parameters for 300−4200 traces. The error bars represent one standard deviation across all the accepted traces analyzed under each condition. (c) Multiple FOV data collection scheme for 1.2 mm diameter 3D-printed wells. A total of 25 FOVs were collected starting from the upper right corner of the sample well. The acquisition time for each FOV is 30 s. After moving to the next FOV, a 7 s delay was used to allow the autofocus system to establish focus before acquiring the next movie. (d) Representative kinetic fingerprint for detecting exon 19 deletion mutation COSM 6223 in a 30 s movie using 400 nM Cy3 FP and 600 nM Cy5 FP. (e) Representative FRET trace from a control sample in the absence of the target strands but containing all the other components of the ATPS-SiMREPS assay. (f and g) Scatterplot of N_{b+d} and $\tau_{bound,\ median}$ for all the traces generated in 25 FOVs (30 s/FOV) collected in samples in the presence (f) or absence (g) of exon 19 deletion COSM 6223 mutant dsDNA (160 bp). Dashed lines indicate the threshold for accepting a trace as a positive count for a single exon 19 mutant dsDNA. The black dots represent the traces that did not pass the filtering criteria and were thus not counted as target mutant dsDNA molecules. The red dots represent the traces that pass the filtering criteria and were accepted to be counted as target mutant dsDNA molecules. (h) Comparison of the accepted counts obtained upon using the initial imaging conditions (100 nM FPs, 10 min/FOV, 1 FOV/well, ambient room temperature) and the optimized conditions (400 nM Cy3 FP, 600 nM Cy5 FP, 30 s/FOV, 25 FOV/well, 27 °C) with and without ATPS. The error bars represent the standard error of the mean for three replicates.

faster data acquisition than previous non-FRET SiMREPS assays. This in turn is expected to facilitate either (1) faster data acquisition, and/or (2) further increased sensitivity by permitting the imaging of more FOVs in the same amount of time, thus detecting a larger fraction of captured target molecules than would be possible with a single FOV.

To test these hypotheses, using an initial target concentration of 100 fM we systematically optimized the imaging temperature and FP concentrations to shorten the acquisition time per FOV required to observe a number of binding and dissociation events per trace (N_{b+d}) that is sufficient to distinguish specific and nonspecific binding. First, we sought to increase the rate of probe dissociation to permit more FP binding events to occur within a given observation time. We found that elevating the imaging temperature from 24 to 28 °C increased N_{b+d} and decreased the median bound (high-FRET) dwell time, while not significantly affecting the median unbound (low-FRET) dwell time (Figure 5a), presumably by destabilizing the hybridization between the FPs and the target strand or auxiliary strand. Second, we sought to increase the rate of binding by increasing the concentrations of the two FPs used during imaging. We found that increasing the FP concentration from 100 to 600 nM significantly increased N_{b+d} and decreased the median unbound dwell time at a fixed imaging temperature (27 °C), while not affecting the median bound dwell time significantly (Figure 5b). For the final

https://doi.org/10.1021/acssensors.2c00135
ACS Sens. 2022, 7, 1419−1430

version of the assay, we selected a combination of 400 nM Cy3 and 600 nM Cy5 FP and an imaging temperature of 27 °C. Using these optimized conditions, we were able to shorten the acquisition time from 10 min to 30 s per FOV (i.e., a 20-fold reduction) while remaining able to distinguish the distinctive kinetic fingerprints of the exon 19 deletion sequence from nonspecific FP binding (Figure 5d,e). This reduction in acquisition time enabled us to detect captured targets across nearly the entire slide capture surface in one sample well (1.2 mm in diameter) in less than 20 min, using the scanning pattern shown in Figure 5c.

To validate our ATPS-enhanced FRET-SiMREPS assay under these optimized conditions, we performed measurements over 25 FOVs per well in samples containing or lacking of 10 fM target exon 19 deletion dsDNA. Kinetic threshold parameters for selecting valid target traces were optimized to achieve the maximum positive counts in the sample and the minimum false signals in a target-free control (Figure 5f,g). The multiple-FOV data acquisition enabled by the shortened imaging time permitted the detection of approximately 27-fold more target molecules than the initial imaging conditions, independent of the sensitivity improvement provided by the ATPS (Figure 5h). By combining the ATPS approach with the measurement of 25 FOVs, the single molecule count increased by a factor of approximately 450 from ~58 to ~26 000 at 100 fM initial COSM 6223 mutant dsDNA concentration, consistent with a corresponding increase in sensitivity (Figure 5h).

Ultrasensitive Detection of Mutant dsDNA Using ATPS-Assisted FRET-SiMREPS. Next, we aimed to test the sensitivity of our optimized, ATPS-enhanced FRET-SiMREPS assay against our two clinically relevant *EGFR* tyrosine kinase domain in-frame deletion mutations COSM 6223 and COSM 6225. First, we obtained standard curves for detecting the ~160 bp synthetic mutant dsDNAs in a 1× PBS buffer with or without the application of ATPS. The total SiMREPS signal counts across 25 FOVs exhibit a linear dependence on the concentration of target mutant dsDNA over 3 orders of magnitude (Figure 6a,b). The calculated limit of detection (LOD) when using ATPS is approximately 18-fold lower (more sensitive) compared to the LOD obtained from the standard curve for target samples without ATPS and >300 fold lower than the previously reported LOD in the absence of both ATPS and rapid 25-FOV imaging.[14] We attribute this drastic improvement in the detection sensitivity of SiMREPS assays almost equally to the target enrichment by ATPS and the multiple-FOV data collection.

To further test the assay's specificity, we spiked either COSM 6223 or COSM 6225 mutant dsDNA at varying concentrations into a solution containing a high excess (10 pM) of exon 19 wild-type (WT) dsDNA to obtain a second set of standard curves and calculate LODs. These standard curves again showed a clear linear correlation between the SiMREPS counts and the contrived mutant concentrations in the presence of this high WT DNA background (Figure 6c,d). Although the LODs were higher than those obtained only in buffer, they remained in the lower attomolar range. The slight increase in LOD was likely caused by three main factors: (1) the high amount of WT DNA competing with mutant DNA for capture probe sites on the surface during capture; (2) the increased background from binding of Cy3 FPs to the auxiliary probes that bound to surface-captured WT DNA resulted in a lower signal-to-noise ratio (S/N); (3) a small number of false

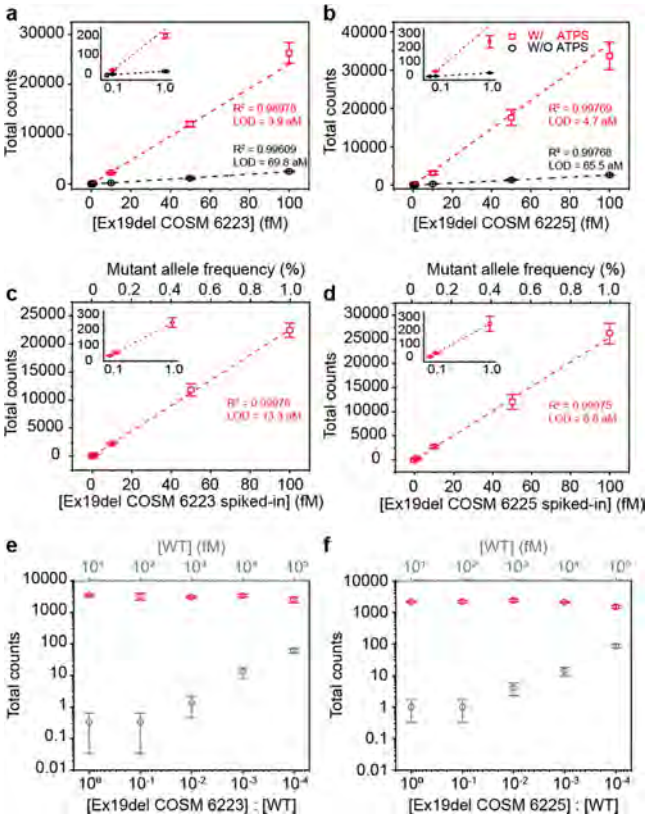

Figure 6. Quantification of varying concentrations of exon 19 deletion mutations COSM 6223 and COSM 6225 in a PBS buffer and spiked into a constant excess of 10 pM exon 19 wild-type DNA, as well as constant mutant dsDNA spiked into a varying excess of exon 19 wild-type DNA. (a and b) Standard curves for exon 19 deletion mutation COSM 6223 (a) and COSM 6225 (b) in a buffer with (red) and without (black) an ATPS target enrichment step. Data points represent the mean ± SEM of three independent measurements. Total counts obtained from 25 FOVs per sample were used for each measurement. An error-weighted linear regression (red and black dashed lines) was fit to each standard curve with the *y*-intercept constrained to the mean counts of blank controls. The slopes of the linear fits are 240.07 and 24.82 (368.38 and 26.41) for the standard curves of exon 19 deletion mutation COSM 6223 (COSM 6225) with and without use of the ATPS. (c and d) Standard curves for the exon 19 deletion mutations COSM 6223 (c) and COSM 6225 (d) in a constant background of 10 pM exon 19 wild-type DNA with an ATPS enrichment step. Data points represent the mean ± SEM of three independent measurements. Total counts obtained from 25 FOVs per sample were used for each measurement. An error-weighted linear regression (red dashed lines) was fit to the standard curves. The slopes of the linear fits are 225.56 and 253.56 for COSM 6223 and COSM 6225, respectively. (e and f) Quantification of 10 fM exon 19 deletion mutation COSM 6223 (e) and COSM 6225 (f) spiked into 100 pM, 10 pM, 1 pM, 100 fM or 10 fM exon 19 wild-type DNA. The top *x*-axis represents the concentration of exon 19 wild-type DNA and the bottom *x*-axis represents the mutant:wild-type ratio. The red data points represent the mean ± SEM of the total counts for mutant dsDNA of three independent measurements. The gray data points represent the mean ± SEM of the total false positives for samples containing only exon 19 wild-type DNA of three independent measurements.

positive counts induced by spurious binding of FPs to WT DNA exhibited similar binding kinetics to FPs binding to mutant target DNA. To suppress the binding of WT DNA to surface capture sites, we designed a WT blocker DNA (24 nt)

https://doi.org/10.1021/acssensors.2c00135
ACS Sens. 2022, 7, 1419−1430

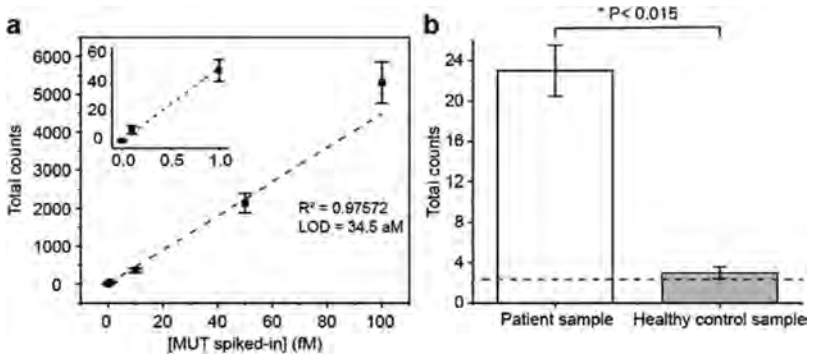

Figure 7. Quantification and validation of an assay for exon 19 deletion mutant dsDNA spiked into healthy plasma cfDNA and endogenous exon 19 deletion mutant DNA in blood cfDNA from a lung cancer patient. (a) Standard curve of varying concentrations of exon 19 deletion COSM 6225 mutant dsDNA (160 bp) spiked into 7 ng of healthy plasma cfDNA. Data points represent the mean ± SEM of three independent measurements. Total counts from 81 FOVs per sample were used for each measurement (Figure S7). An error-weighted linear regression (black dashed line) was fit to the standard curve, yielding a slope of 44.875. (b) Validation of ATPS-SiMREPS assay for COSM 6225 in cfDNA extracted from a lung cancer patient clinical blood sample. A total of three replicates were performed for each sample. The input of the total cfDNA was 7 ng per replicate. Patient sample: 23 ± 3 counts and healthy control sample: 3 ± 1 counts. A *t*-test (two-tailed and unpaired) was performed to evaluate the statistical significance of the difference between the results, yielding $p = 0.012$, representing >98.5% confidence that the two results are significantly different. The dashed line represents the background signal plus 3 s.d. of the background signal from the standard curve in panel a.

that can stably bind to the WT DNA sequence but not to the mutant sequences. The 9 nt segment of the 3′ end of the WT blocker is complementary to both WT and mutant DNA sequence, while also covering 4 nt of the capture region. The WT blocker was thus expected to inhibit capture of the WT DNA due to the partial blocking of the capture region in WT DNA sequences. Indeed, with the inclusion of WT blocker we obtained much clearer fluorescence images with improved S/N for mutant dsDNA spiked into WT (Figures S4 and S5).

Detection specificity for the two exon 19 deletion mutations was then examined by spiking mutant dsDNA of constant concentration (10 fM) into samples containing an increasing excess of exon 19 WT dsDNA. A specificity of >99.999% was achieved for both mutant dsDNAs that, while quite high, was somewhat lower than the specificity reported previously in the absence of ATPS. This may be attributed to the fact that the ATPS enrichment step concentrates every DNA sequence into the bottom salt-rich phase of the polymer−salt ATPS, leading to higher capture efficiency of target molecules but also causing larger interference from the large excess of WT DNA. Consistent with this notion, with increasing in the WT DNA concentration, the false positive counts rose and the true positive counts decreased slightly (Figure 6e,f). An experiment of spiking an even lower amount of mutant dsDNA (0.1 fM) into 0.1 fM−1 pM WT dsDNA was also conducted to represent a more biologically meaningful scenario. In that case, the amount of total accepted counts remains the same as increasing the WT DNA concentrations and the false positive counts from WT controls are minimal (Figure S6).

ATPS-Assisted FRET-SiMREPS Validation by Contrived and Clinical Samples of Mutant dsDNA. To examine the performance of our ATPS-enhanced FRET-SiMREPS assay in detecting circulating tumor DNA in a matrix of cell-free DNA (cfDNA) extracted from human biofluids, we further validated it by quantifying 160 bp synthetic mutant dsDNA spiked into cfDNA extracted from the pooled blood plasma of six healthy donors. A linear correlation ($R^2 > 0.975$) was observed between SiMREPS signal and the concentration of mutant dsDNA spiked into 7 ng of healthy plasma cfDNA (Figure 7a). However, the total accepted counts in all healthy plasma spiked-in samples were about 4- to 5-fold lower than in pure buffer or in WT DNA spiked-in samples. We interpret this as interference from the large excess of cfDNA molecules that may compete with the surface capture of mutant dsDNA, as well as the application of stricter kinetic filtering criteria required to eliminate nearly all false positives in this matrix.

Finally, to test the robustness of the ATPS-assisted, FRET-based SiMREPS assay and its potential utility in more clinically relevant samples, we detected endogenous ctDNAs in a cancer patient sample containing the exon 19 deletion mutation COSM 6225 and compared the obtained SiMREPS signal with that of a negative control containing cfDNAs from the blood plasma of healthy donors. The difference in the SiMREPS signal is significant with a confidence level >99.8% ($P < 0.015$), indicating that our amplification-free assay can detect the low concentrations of endogenous ctDNA present in biofluids from cancer patients (Figure 7b).

CONCLUSION

We here have shown that phase separation by an ATPS can be used to greatly improve the sensitivity of a surface-based assay by enhancing the mass transport of analyte molecules to assay surfaces, concentrating them into a small volume near the surface and improving capture efficiency. By combining this ATPS approach with the rapid multi-FOV imaging enabled by FRET-SiMREPS, we have shown that the sensitivity of an assay for two clinically relevant cancer mutations can be increased by as much as 300-fold, permitting the amplification-free detection of the small amounts of circulating tumor DNA present in cfDNA isolated from patient blood samples. This amplification-free detection was also facilitated by our use of short oligonucleotide tiles during heat-denaturation to inhibit unwanted duplex formation in the target strand (e.g., secondary structure or rehybridization with its complement), which allowed the sensitive detection of the ∼160 bp DNA fragments typically seen in cfDNA samples. This may be a useful strategy for the detection of other relatively long nucleic acid analytes, such as long noncoding RNAs (lncRNAs), with SiMREPS and other methods that employ probe hybridization close to room temperature.

The application of a PEG-citrate-NaCl ATPS in this study improved the estimated capture efficiency of the model

https://doi.org/10.1021/acssensors.2c00135
ACS Sens. 2022, 7, 1419−1430

SiMREPS assay from ∼1% to ∼18% by concentrating the target DNA molecules into a very small volume (<1 μL) near the assay surface, thus reducing the distance analytes must travel to reach the surface. Importantly, a small sample volume of 10 μL is sufficient to achieve high (low attomolar) detection sensitivity when using ATPS as a target enrichment step. In addition, our optimized FRET-based SiMREPS approach allows for the rapid imaging of many FOVs, thus permitting detection of a larger fraction of captured analyte molecules. The FRET approach enables the use of higher FP concentrations, thus achieving more binding events per minute and accelerating the acquisition of kinetic fingerprinting data. Control of sample temperature during imaging is also crucial because lower temperatures can slow down the transient binding of FPs, while higher temperatures can result in binding events that are too short to detect and potentially result in significant dissociation of the analyte from the capture probe. The efficient detection of captured analytes was also facilitated by the use of 3D-printed sample wells with small openings that focus a thin layer of the target-rich phase onto a region of the assay surface only 1.2 or 2 mm in diameter, a large fraction of which can be rapidly imaged using the FRET-SiMREPS probe strategy.

Compared to other methods of concentrating analytes, such as electrokinetic focusing, microfluidics, and magnetic beads, ATPS offers a simple and robust way to enhance the target capture efficiency and, thus, the sensitivity of surface-based assays. Although the present work concerns a single-molecule DNA assay, we expect that such an ATPS can be applied to other surface-based bioassays, including those of other types of analytes such as proteins, which have been shown to partition more readily to the PEG-rich phase in a PEG-salt ATPS with the presence of higher concentration of NaCl (8.8% w/w), or to the dextran-rich phase in a PEG-dextran ATPS, affected more by the charge of proteins at lower concentration of NaCl (i.e., 0.6% w/w).[33]

In the future, the application of ATPS-enhanced surface capture to assays of other target sequences, other sample types (e.g., trans-renal DNA in urine), and analyte types (e.g., proteins) should be explored. In addition, the development and optimization of strategies to better mitigate interference from other, nontarget analytes that are enriched by the ATPS will broaden the applicability of this approach. This might be achieved by further optimizing strategies for reducing the capture of sequences other than the target sequence, such as the WT blocker we employed, or by optimization of the capture probe or conditions (temperature, salt-rich phase composition) to reduce nonspecific interactions with the capture probe, analyte, or imaging surface during analyte capture. We expect that the use of ATPS-enhanced surface capture will improve the sensitivity of a wide range of surface-based assays for nucleic acids and other analytes in research and clinical diagnostics.

■ ASSOCIATED CONTENT

Supporting Information

The Supporting Information is available free of charge at https://pubs.acs.org/doi/10.1021/acssensors.2c00135.

Cloud point titration assay, UV−vis spectroscopy measurement of enriched DNA in ATPS, impact of tiles (short oligonucleotides complementary to part of target sequence) on the detection of long target dsDNA, ATPS enrichment for enhanced target surface capture, impact of wild-type blocker on improving imaging background and S/N ratio of accepted traces, quantification of MUT counts (0.1 fM) at varying MUT:WT molar ratios, 81-FOV data collection pattern in 2 mm-diameter 3D-printed sample wells, and list of oligonucleotides for SiMREPS assay construct in this study (PDF)

■ AUTHOR INFORMATION

Corresponding Authors

Muneesh Tewari − *Department of Internal Medicine, Division of Hematology/Oncology, Center for RNA Biomedicine, Department of Biomedical Engineering, and Center for Computational Medicine and Bioinformatics, University of Michigan, Ann Arbor, Michigan 48109, United States*; Email: mtewari@med.umich.edu

Alexander Johnson-Buck − *Single Molecule Analysis Group, Department of Chemistry, Department of Internal Medicine, Division of Hematology/Oncology, and Center for RNA Biomedicine, University of Michigan, Ann Arbor, Michigan 48109, United States*; orcid.org/0000-0003-3748-6000; Email: alebuck@umich.edu

Nils G. Walter − *Single Molecule Analysis Group, Department of Chemistry, Center for RNA Biomedicine, and Center for Computational Medicine and Bioinformatics, University of Michigan, Ann Arbor, Michigan 48109, United States*; orcid.org/0000-0002-7301-1275; Email: nwalter@umich.edu

Authors

Zi Li − *Single Molecule Analysis Group, Department of Chemistry, University of Michigan, Ann Arbor, Michigan 48109, United States*

Molly McNeely − *Single Molecule Analysis Group, Department of Chemistry, University of Michigan, Ann Arbor, Michigan 48109, United States*

Erin Sandford − *Department of Internal Medicine, Division of Hematology/Oncology, University of Michigan, Ann Arbor, Michigan 48109, United States*; orcid.org/0000-0003-3498-8144

Complete contact information is available at: https://pubs.acs.org/10.1021/acssensors.2c00135

Notes

The authors declare the following competing financial interest(s): A.J.-B., M.T., and N.G.W. are inventors on multiple patent applications related to SiMREPS, and equity holders of aLight Sciences Inc., a startup company aiming to commercialize the presented technology.

■ ACKNOWLEDGMENTS

We thank Dr. Damon Hoff of the Single Molecule Analysis in Real-Time (SMART) Center at the University of Michigan for assistance and advice with instrumentation and Dr. Shuichi Takayama, now at the Georgia Institute of Technology, for initial brainstorming on possible pre-concentration strategies. This work was supported by R33 CA229023 (N.G.W. and M.T.).

■ ABBREVIATIONS

ATPS, aqueous two-phase system; SiMREPS, single-molecule recognition through equilibrium Poisson sampling; FRET, Förster resonance energy transfer; Cy3, cyanine 3; Cy5, cyanine 5; OSS, oxygen scavenging system; cfDNA, cell-free DNA; FOV, field of view; LOD, limit of detection

■ REFERENCES

(1) Sassolas, A.; Leca-Bouvier, B. D.; Blum, L. J. DNA Biosensors and Microarrays. *Chem. Rev.* **2008**, *108*, 109−139.

(2) (a) Chen, Z. Q.; Dodig-Crnkovic, T.; Schwenk, J. M.; Tao, S. C. Current Applications of Antibody Microarrays. *Clin. Proteom.* **2018**, *15*. DOI: 10.1186/s12014-018-9184-2. (b) Duarte, J. G.; Blackburn, J. M. Advances in the Development of Human Protein Microarrays. *Expert Rev. Proteomics.* **2017**, *14*, 627−641.

(3) Lequin, R. M. Enzyme Immunoassay (EIA)/Enzyme-Linked Immunosorbent Assay (ELISA). *Clin. Chem.* **2005**, *51*, 2415−2418.

(4) de Avila, B. E. F.; Watkins, H. M.; Pingarron, J. M.; Plaxco, K. W.; Palleschi, G.; Ricci, F. Determinants of the Detection Limit and Specificity of Surface-Based Biosensors. *Anal. Chem.* **2013**, *85*, 6593−6597.

(5) Buermans, H. P. J.; den Dunnen, J. T. Next Generation Sequencing Technology: Advances and Applications. *Biochim Biophys Acta Mol. Basis Dis* **2014**, *1842*, 1932−1941.

(6) Eid, J.; Fehr, A.; Gray, J.; Luong, K.; Lyle, J.; Otto, G.; Peluso, P.; Rank, D.; Baybayan, P.; Bettman, B.; et al. Real-Time DNA Sequencing from Single Polymerase Molecules. *Science* **2009**, *323*, 133−138.

(7) Cheng, F. F.; Su, L.; Qian, C. Circulating Tumor DNA: A Promising Biomarker in the Liquid Biopsy of Cancer. *Oncotarget* **2016**, *7*, 48832−48841.

(8) Huertas, C. S.; Calvo-Lozano, O.; Mitchell, A.; Lechuga, L. M. Advanced Evanescent-Wave Optical Biosensors for the Detection of Nucleic Acids: An Analytic Perspective. *Front. Chem.* **2019**, *7*. DOI: 10.3389/fchem.2019.00724.

(9) (a) Huang, S. H.; Chang, Y. S.; Juang, J. M. J.; Chang, K. W.; Tsai, M. H.; Lu, T. P.; Lai, L. C.; Chuang, E. Y.; Huang, N. T. An Automated Microfluidic DNA Microarray Platform for Genetic Variant Detection in Inherited Arrhythmic Diseases. *Analyst* **2018**, *143*, 1367−1377. (b) Chung, Y. C.; Lin, Y. C.; Shiu, M. Z.; Chang, W. N. T. Microfluidic Chip for Fast Nucleic Acid Hybridization. *Lab Chip.* **2003**, *3*, 228−233.

(10) Nguyen, H. T.; Trouillon, R.; Matsuoka, S.; Fiche, M.; de Leval, L.; Bisig, B.; Gijs, M. A. M. Microfluidics-Assisted Fluorescence In Situ Hybridization for Advantageous Human Epidermal Growth Factor Receptor 2 Assessment in Breast Cancer. *Lab. Invest.* **2017**, *97*, 93−103.

(11) (a) Zhang, J. L.; Wang, Y.; Wong, T. I.; Liu, X. H.; Zhou, X. D.; Liedberg, B. Electrofocusing-Enhanced Localized Surface Plasmon Resonance Biosensors. *Nanoscale* **2015**, *7*, 17244−17248. (b) Garcia-Guirado, J.; Rica, R. A.; Ortega, J.; Medina, J.; Sanz, V.; Ruiz-Reina, E.; Quidant, R. Overcoming Diffusion-Limited Biosensing by Electrothermoplasmonics. *ACS Photonics* **2018**, *5*, 3673−3679.

(12) Potapov, V.; Ong, J. L. Examining Sources of Error in PCR by Single-Molecule Sequencing. *PloS One* **2017**, *12*, e0169774.

(13) Hofreiter, M.; Jaenicke, V.; Serre, D.; von Haeseler, A.; Paabo, S. DNA Sequences From Multiple Amplifications Reveal Artifacts Induced by Cytosine Deamination in Ancient DNA. *Nucleic Acids Res.* **2001**, *29*, 4793−4799.

(14) Hayward, S. L.; Lund, P. E.; Kang, Q.; Johnson-Buck, A.; Tewari, M.; Walter, N. G. Ultraspecific and Amplification-Free Quantification of Mutant DNA by Single-Molecule Kinetic Fingerprinting. *J. Am. Chem. Soc.* **2018**, *140*, 11755−11762.

(15) (a) Scherczinger, C. A.; Ladd, C.; Bourke, M. T.; Adamowicz, M. S.; Johannes, P. M.; Scherczinger, R.; Beesley, T.; Lee, H. C. A Systematic Analysis of PCR Contamination. *J. Forensic Sci.* **1999**, *44*, 1042−1045. (b) Aslanzadeh, J. Preventing PCR Amplification Carryover Contamination in a Clinical Laboratory. *Ann. Clin. Lab. Sci.* **2004**, *34*, 389−396.

(16) (a) Cohen, L.; Hartman, M. R.; Amardey-Wellington, A.; Walt, D. R. Digital direct detection of microRNAs using single molecule arrays. *Nucleic Acids Res.* **2017**, *45*, e137. (b) Veldman-Jones, M. H.; Brant, R.; Rooney, C.; Geh, C.; Emery, H.; Harbron, C. G.; Wappett, M.; Sharpe, A.; Dymond, M.; Barrett, J. C.; et al. Evaluating Robustness and Sensitivity of the NanoString Technologies nCounter Platform to Enable Multiplexed Gene Expression Analysis of Clinical Samples. *Cancer Res.* **2015**, *75*, 2587−2593. (c) Geiss, G. K.; Bumgarner, R. E.; Birditt, B.; Dahl, T.; Dowidar, N.; Dunaway, D. L.; Fell, H. P.; Ferree, S.; George, R. D.; Grogan, T.; et al. Direct multiplexed measurement of gene expression with color-coded probe pairs. *Nat. Biotechnol.* **2008**, *26*, 709−709. (d) Geiss, G. K.; Bumgarner, R. E.; Birditt, B.; Dahl, T.; Dowidar, N.; Dunaway, D. L.; Fell, H. P.; Ferree, S.; George, R. D.; Grogan, T.; et al. Direct multiplexed measurement of gene expression with color-coded probe pairs. *Nat. Biotechnol.* **2008**, *26*, 317−325.

(17) Martins, D.; Wei, X.; Levicky, R.; Song, Y. A. Accelerating the Mass Transport OF DNA Biomolecules onto DNA Microarray for Enhanced Detection by Electrokinetic Concentration in a Microfluidic Chip. In *Proceedings of the Asme 5th International Conference on Micro/Nanoscale Heat and Mass Transfer*; ASME, 2016; Vol. *1*.

(18) (a) Iqbal, M.; Tao, Y. F.; Xie, S. Y.; Zhu, Y. F.; Chen, D. M.; Wang, X.; Huang, L. L.; Peng, D. P.; Sattar, A.; Shabbir, M. A.; et al. Aqueous Two-Phase System (ATPS): an Overview and Advances in its Applications. *Biol. Proced. Online* **2016**, *18*. DOI: 10.1186/s12575-016-0048-8. (b) Chao, Y. C.; Shum, H. C. Emerging Aqueous Two-Phase Systems: From Fundamentals of Interfaces to Biomedical Applications. *Chem. Soc. Rev.* **2020**, *49*, 114−142.

(19) Luechau, F.; Ling, T. C.; Lyddiatt, A. Partition of Plasmid DNA in Polymer-Salt Aqueous Two-Phase Systems. *Sep. Purif. Technol.* **2009**, *66*, 397−404.

(20) (a) Mao, L. N.; Rogers, J. K.; Westoby, M.; Conley, L.; Pieracci, J. Downstream Antibody Purification Using Aqueous Two-Phase Extraction. *Biotechnol. Prog.* **2010**, *26*, 1662−1670. (b) Azevedo, A. M.; Gomes, A. G.; Rosa, P. A. J.; Ferreira, I. F.; Pisco, A.; Aires-Barros, M. R. Partitioning of Human Antibodies in Polyethylene Glycol-Sodium Citrate Aqueous Two-Phase Systems. *Sep. Purif. Technol.* **2009**, *65*, 14−21.

(21) (a) Gomes, G. A.; Azevedo, A. M.; Aires-Barros, M. R.; Prazeres, D. M. F. Purification of Plasmid DNA with Aqueous Two Phase Systems of PEG 600 and Sodium Citrate/Ammonium Sulfate. *Sep. Purif. Technol.* **2009**, *65*, 22−30. (b) Rahimpour, F.; Feyzi, F.; Maghsoudi, S.; Hatti-Kaul, R. Purification of Plasmid DNA with Polymer-Salt Aqueous Two-Phase system: Optimization Using Response Surface Methodology. *Biotechnol. Bioeng.* **2006**, *95*, 627−637.

(22) Frampton, J. P.; White, J. B.; Simon, A. B.; Tsuei, M.; Paczesny, S.; Takayama, S. Aqueous Two-Phase System Patterning of Detection Antibody Solutions for Cross-Reaction-Free Multiplex ELISA. *Sci. Rep.* **2015**, *4*, 4878.

(23) Johnson-Buck, A.; Su, X.; Giraldez, M. D.; Zhao, M. P.; Tewari, M.; Walter, N. G. Kinetic Fingerprinting to Identify and Count Single Nucleic Acids. *Nat. Biotechnol.* **2015**, *33*, 730−732.

(24) Chatterjee, T.; Knappik, A.; Sandford, E.; Tewari, M.; Strong, W. B.; Thrush, E. P.; Oh, K. J.; Liu, N.; Walter, N. G.; Johnson-Buck, A.; et al. Direct Kinetic Fingerprinting and Digital Counting of Single Protein Molecules. *Proc. Natl. Acad. Sci. U.S.A.* **2020**, *117*, 22815−22822.

(25) Johnson-Buck, A.; Li, J. M.; Tewari, M.; Walter, N. G. A Guide to Nucleic Acid Detection by Single-Molecule Kinetic Fingerprinting. *Methods* **2019**, *153*, 3−12.

(26) (a) Chatterjee, T.; Li, Z.; Khanna, K.; Montoya, K.; Tewari, M.; Walter, N. G.; Johnson-Buck, A. Ultraspecific Analyte Detection by Direct Kinetic Fingerprinting of Single Molecules. *Trac, Trends Anal. Chem.* **2020**, *123*, 115764. (b) Mandal, S.; Li, Z.; Chatterjee, T.; Khanna, K.; Montoya, K.; Dai, L. H.; Petersen, C.; Li, L. D.; Tewari, M.; Johnson-Buck, A.; et al. Direct Kinetic Fingerprinting for High-

https://doi.org/10.1021/acssensors.2c00135
ACS Sens. 2022, 7, 1419−1430

Accuracy Single-Molecule Counting of Diverse Disease Biomarkers. *Acc. Chem. Res.* **2021**, *54*, 388−402.
(27) Norton, S. E.; Lechner, J. M.; Williams, T.; Fernando, M. R. A Stabilizing Reagent Prevents Cell-Free DNA Contamination by Cellular DNA in Plasma During Blood Sample Storage and Shipping as Determined by Digital PCR. *Clin. Biochem.* **2013**, *46*, 1561−1565.
(28) Mandal, S.; Khanna, K.; Johnson-Buck, A.; Walter, N. G. A guide to accelerated direct digital counting of single nucleic acid molecules by FRET-based intramolecular kinetic fingerprinting. *Methods* **2022**, *197*, 63−73.
(29) (a) Prinz, A.; Honig, J.; Schuttmann, I.; Zorn, H.; Zeiner, T. Separation and Purification of Laccases From Two Different Fungi Using Aqueous Two-Phase Xxtraction. *Process Biochem* **2014**, *49*, 335−346. (b) Pavlovic, M.; Plucinski, A.; Zhang, J. R.; Antonietti, M.; Zeininger, L.; Schmidt, B. Cascade Kinetics in an Enzyme-Loaded Aqueous Two-Phase System. *Langmuir* **2020**, *36*, 1401−1408.
(30) Mokhtarani, B.; Karimzadeh, R.; Amini, M. H.; Manesh, S. D. Partitioning of Ciprofloxacin in Aqueous Two-Phase System of Poly(ethylene glycol) and Sodium Sulphate. *Biochem. Eng. J.* **2008**, *38*, 241−247.
(31) (a) Luechau, F.; Ling, T. C.; Lyddiatt, A. Selective Partition of Plasmid DNA and RNA in Aqueous Two-Phase Systems by the Addition of Neutral Salt. *Sep. Purif. Technol.* **2009**, *68*, 114−118. (b) Wessner, M.; Diederich, K.; Brandenbusch, C. Influence of Sodium Chloride and Lithium Bromide on the Phase Behavior of a Citrate-Polyethylene Glycol 2000 Aqueous Two-Phase System. *J. Chem. Eng. Data* **2020**, *65*, 4009−4017.
(32) Schwarzenbach, H.; Hoon, D. S. B.; Pantel, K. Cell-Free Nucleic Acids as Biomarkers in Cancer Patients. *Nat. Rev. Cancer* **2011**, *11*, 426−437.
(33) (a) Asenjo, J. A.; Andrews, B. A. Aqueous Two-Phase Systems for Protein Separation: A Perspective. *J. Chromatogr. A* **2011**, *1218*, 8826−8835. (b) Andrews, B. A.; Schmidt, A. S.; Asenjo, J. A. Correlation for the Partition Behavior of Proteins in Aqueous Two-Phase Systems: Effect of Surface Hydrophobicity and Charge. *Biotechnol. Bioeng.* **2005**, *90*, 380−390.

https://doi.org/10.1021/acssensors.2c00135
ACS Sens. 2022, 7, 1419−1430

Supporting Information

Attomolar Sensitivity in Single Biomarker Counting upon Aqueous Two-Phase Surface Enrichment

Zi Li[†], Molly McNeely[†], Erin Sandford[£], Muneesh Tewari[*,£,§,ψ,¶] , Alexander Johnson-Buck[*,†,£,§], and Nils G. Walter[*,†,§,¶]

[†]Single Molecule Analysis Group, Department of Chemistry, [£]Department of Internal Medicine, Division of Hematology/Oncology, [§]Center for RNA Biomedicine, [ψ] Department of Biomedical Engineering, and [¶]Center for Computational Medicine and Bioinformatics, University of Michigan, Ann Arbor, Michigan, 48109, United States

AUTHOR INFORMATION

Corresponding Authors

*E-mail: mtewari@med.umich.edu

*E-mail: alebuck@umich.edu

*E-mail: nwalter@umich.edu

The manuscript was written based on contributions from all authors.

All authors have given approval to the final version of the manuscript.

CONTENTS

Figures S1-S7

Table S1

1. Cloud Point Titration Assay

The cloud point titration method was used to determine the binodal curve of the ATPS used for improving the capture efficiency of a surface-based SiMREPS assay. Binodal curves are useful in characterizing ATPS and provide information about the system in different states. Two solutions, PEG-rich phase (40% w/w) and sodium citrate-rich phase (40% w/w), were made using PEG-3350 or sodium citrate, phosphate buffered saline (PBS), and varying concentrations of sodium chloride. A third solution of 0.6× PBS was also made. The PEG-rich solution (5 g) was placed into an Erlenmeyer flask. The sodium citrate-based solution was added dropwise until the solution in the flask became cloudy. The 0.6× PBS solution was then added until the solution in the flask became clear again. The weight of the system was measured each time the solution in the flask changed from clear to cloudy. These measurements were then used to calculate % w/w PEG and % w/w sodium citrate and plotted to form the binodal curve in the phase diagram.

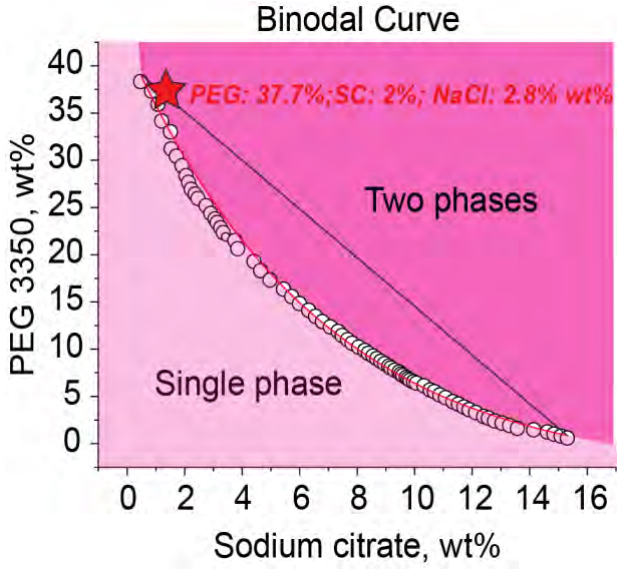

Figure S1 | Phase diagram for a polymer (polyethylene glycol, PEG, MW 3350) and a salt (sodium citrate) system with a binodal curve and a tie line. The region below the binodal curve represents the compositions of those two components that can only form a single phase, while

the region above the binodal curve can form two phases. The red star on the tie line represented the composition of the ATPS that was selected and applied in this study.

2. UV-vis Spectroscopy measurement of enriched DNA in ATPS

Ultraviolet (UV)-visible (vis) spectrophotometry for measuring the concentration of enriched DNA in the salt phase of ATPS was performed using a NanoDrop 2000 spectrophotometer. We first prepared 0.1 μM, 0.25 μM, 0.5 μM and 1 μM target DNA (160-nt, COSMIC ID: COSM 6225) solutions in 1× PBS buffer, and combined 300 μL of each sample to a separate Eppendorf tube containing 222.29 mg of the ATPS master mix, then vortexed and centrifuged to induce phase separation. The blank sample was prepared by adding 300 μL of 1× PBS buffer without any DNA to the Eppendorf tube containing 222.29 mg of the ATPS master mix. Phase separation of the blank sample was also achieved after vortexing and centrifuging. Before measuring the actual ATPS-enriched DNA samples, the blank was taken from the salt phase of the blank phase-separated ATPS sample. To calculate the concentration of enriched DNA in the salt phase, we used the measured absorbance values at a wavelength of 260 nm and the molar extinction coefficient of DNA at 260 nm. Since the concentration of DNA present in PEG phase was not detectable by UV-vis spectrophotometry, we were not able to obtain the partition coefficient empirically using this method.

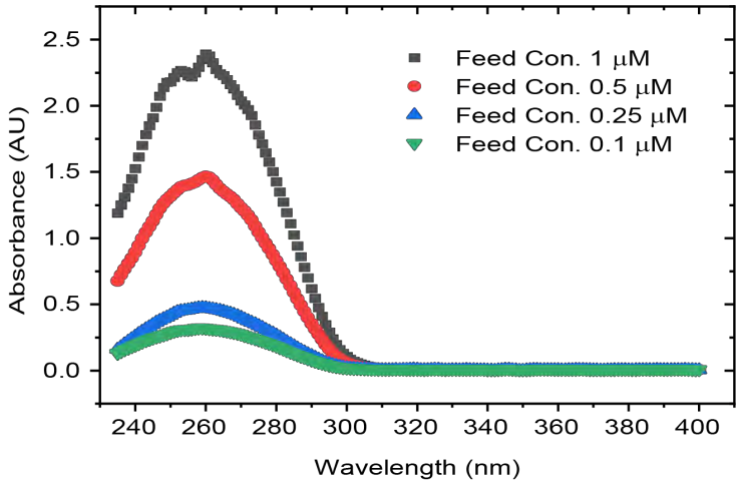

Figure S2 | UV-vis spectra of enriched-DNA in the salt phase of ATPS with feed concentrations of 0.1 μM, 0.25 μM, 0.5 μM and 1 μM. The absorbance value and the molar extinction coefficient of the DNA at 260 nm were used to calculate the concentration of enriched DNA in the salt phase.

3. The Impact of Tiles (Short Oligonucleotides Complementary to Part of Target Sequence) on the Detection of Long Target dsDNA

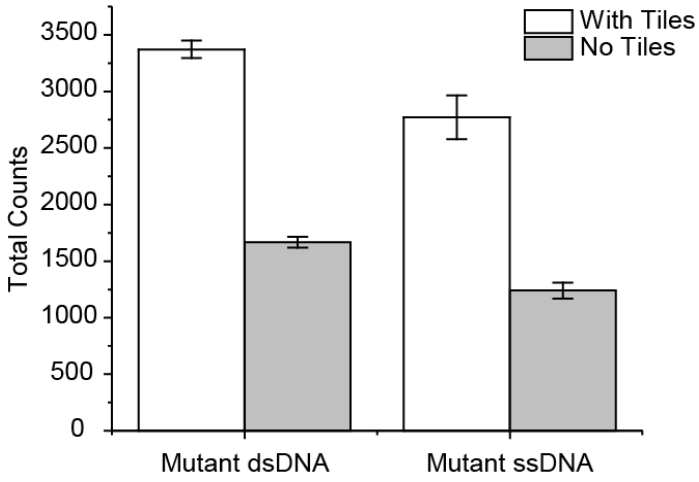

Figure S3 | Impact of tiles (short DNA oligonucleotides) and DNA strandedness (double-stranded, ds, or single-stranded, ss) on the number of total detected molecules (counts) for 10 fM of the

MUT target DNA (exon 19 deletion mutation, COSM 6225) used in this study. Data are presented as means ± SEM of three independent measurements.

4. ATPS Enrichment for Enhanced Target Surface Capture

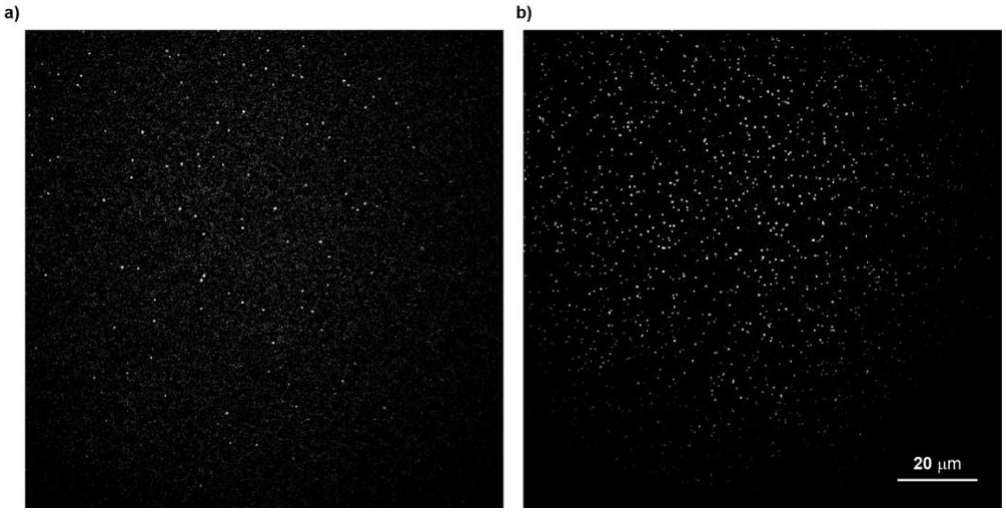

Figure S4 | Comparison of spot density of captured and detected target molecules without a) and with b) the application of ATPS for 100 fM MUT dsDNA (exon 19 deletion mutation, COSM 6225) target sample. The images were called intensity fluctuation map, which were obtained after the first step of SiMREPS data analysis where the average absolute frame-to-frame change in intensity at each pixel was determined and the repeated probe binding and dissociation events were identified. The bright spots represent the repeated binding and dissociation of the fluorescent probes at each location.

5. The Impact of Wild-Type Blocker on Improving Imaging Background and Signal to Noise Ratio (S/N) of Accepted Traces.

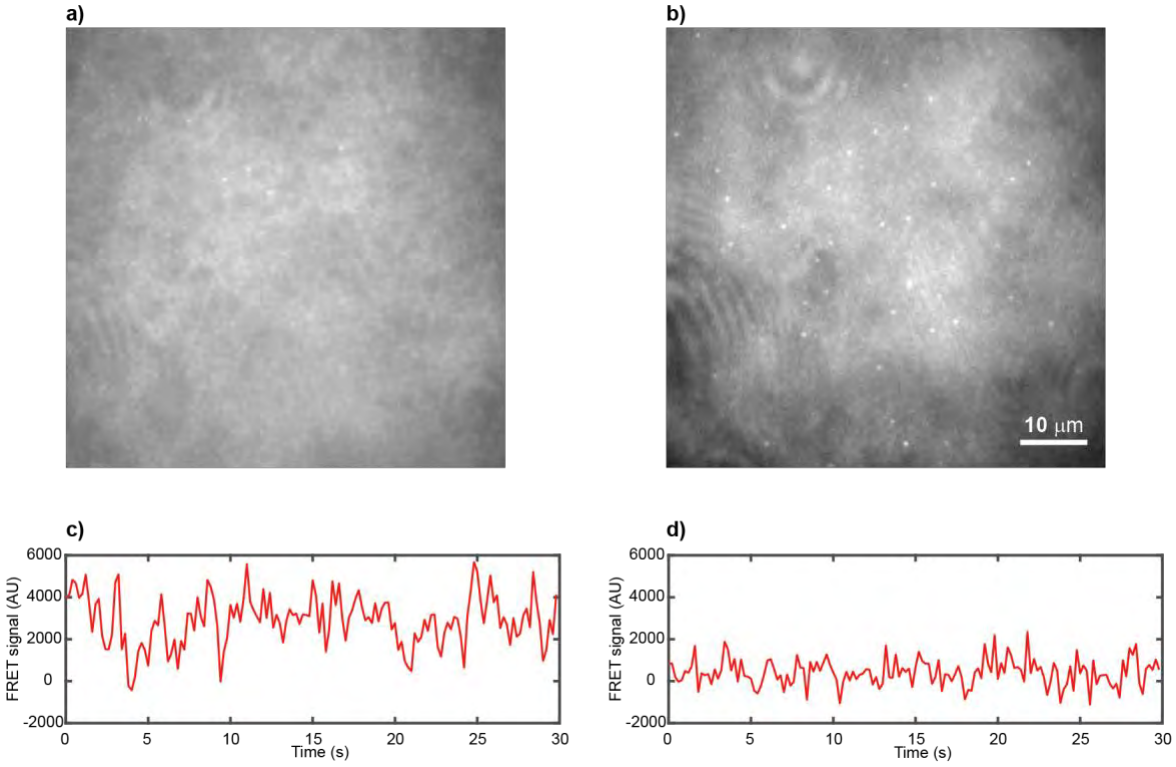

Figure S5 | Wild-type blocker (WTB) can largely block the binding of wild-type (WT) DNA to the surface and subsequently suppress the background and improve the signal to noise ratio during detection. Fluorescence images of one frame for detecting MUT spiked into 10 pM WT DNA a) in the absence and b) in the presence of 10 nM WTB. Representative background traces c) in the absence and d) in the presence of 10 nM WTB, extracted from the movies used to show the fluorescence images in a) and b).

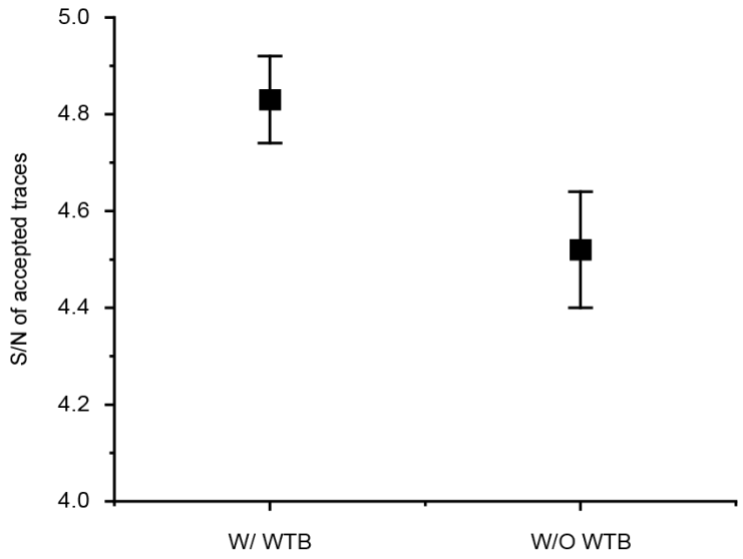

Figure S6 | Signal to noise ratio (S/N) of accepted traces for 10 fM MUT dsDNA (COSM 6223) spiked into 10 pM WT dsDNA with the presence and absence of 10 nM WT blockers (WTB). Data are presented as means ± SD of three independent measurements. Each independent measurement contains 2500 – 4300 accepted traces to obtain a mean S/N value. The threshold for S/N of trace is set to be 2 for both conditions (W/ and W/O WTB).

6. Quantification of MUT counts (0.1 fM) at varying MUT:WT molar ratios

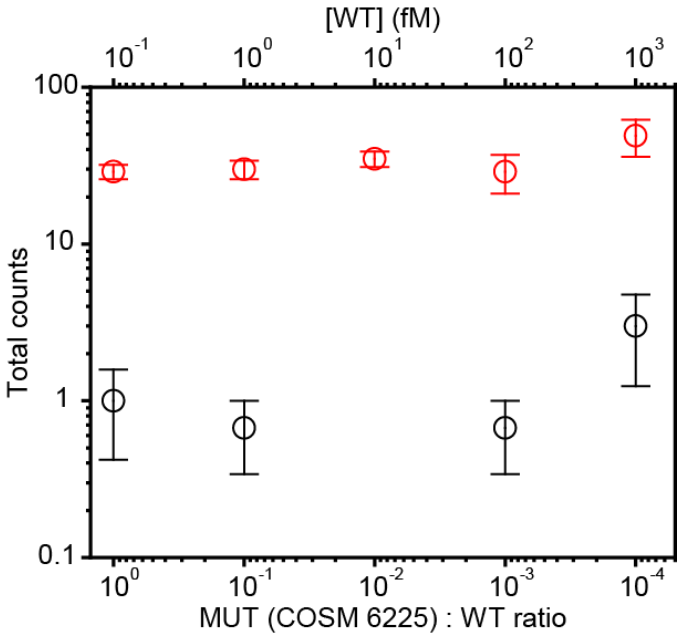

Figure S7 | Quantification of 0.1 fM exon 19 deletion mutation COSM 6225 spiked into 1 pM, 100 fM, 10 fM, 1 fM or 0.1 fM of exon 19 wild-type DNA. The top x-axis represents the concentration of exon 19 wild-type DNA and the bottom x-axis represents the mutant:wild-type ratio. The red data points represent the mean ± SEM of the total counts for mutant dsDNA of three independent measurements. The black data points represent the mean ± SEM of the total false positives for samples containing only exon 19 wild-type DNA of three independent measurements. No data point is shown for 10 fM WT DNA sample, because there is no accepted traces across all three independent measurements.

7. 81-FOV data collection pattern in 2 mm-diameter 3D-printed sample wells.

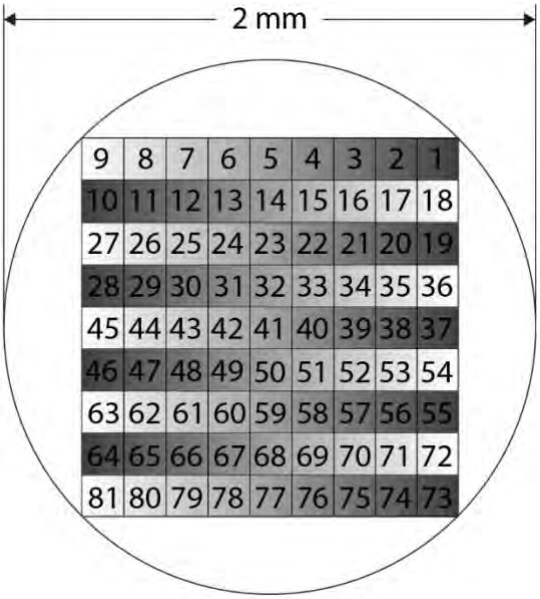

Figure S8 | Illustration of multiple field-of-view (FOV) data collection for 2 mm diameter 3D printed sample wells. The numbers in each square represent the order of the FOV across one sample is being collected, starting from the upper right corner and a total of 81 FOVs are collected. The acquisition time of each FOV is 30 seconds.

Table S1 | List of oligonucleotides for SiMREPS assay construct in this study

Name	Sequence: 5' – 3'
LNA capture probe	+AG+CG+ACG+GG+AA/Biotin TEG/
EGFR Exon 19 deletion, COSM 6223 MUT 160 nt Synthetic DNA, forward	GTC TTC CTT CTC TCT CTG TCA TAG GGA CTC TGG ATC CCA GAA GGT GAG AAA GTT AAA ATT CCC GTC GCT ATC AAA ACA TCT CCG AAA GCC AAC AAG GAA ATC CTC GAT GTG AGT TTC TGC TTT GCT GTG TGG GGG TCC ATG GCT CTG AAC CTC ATA
EGFR Exon 19 deletion, COSM 6223 MUT 160 nt Synthetic DNA, reverse	GTC CTA TGA GGT TCA GAG CCA TGG ACC CCC ACA CAG CAA AGC AGA AAC TCA CAT CGA GGA TTT CCT TGT TGG CTT TCG GAG ATG TTT TGA TAG CGA CGG GAA TTT TAA CTT TCT CAC CTT CTG GGA TCC AGA GTC CCT ATG ACA GAG AGA GAA GGA
EGFR Exon 19 deletion, COSM 6225 MUT 160 nt Synthetic DNA, forward	GTC TTC CTT CTC TCT CTG TCA TAG GGA CTC TGG ATC CCA GAA GGT GAG AAA GTT AAA ATT CCC GTC GCT ATC AAG ACA TCT CCG AAA GCC AAC AAG GAA ATC CTC GAT GTG AGT TTC TGC TTT GCT GTG TGG GGG TCC ATG GCT CTG AAC CTC ATA GGA
EGFR Exon 19 deletion, COSM 6225 MUT 160 nt Synthetic DNA, reverse	GTC CTA TGA GGT TCA GAG CCA TGG ACC CCC ACA CAG CAA AGC AGA AAC TCA CAT CGA GGA TTT CCT TGT TGG CTT TCG GAG ATG TGT TGA TAG CGA CGG GAA TTT TAA CTT TCT CAC CTT CTG GGA TCC AGA GTC CCT ATG ACA GAG AGA GAA GGA AG

EGFR Exon 19 wild-type 160 nt Synthetic DNA, forward	TTC CTT CTC TCT CTG TCA TAG GGA CTC TGG ATC CCA GAA GGT GAG AAA GTT AAA ATT CCC GTC GCT ATC AAG GAA TTA AGA GAA GCA ACA TCT CCG AAA GCC AAC AAG GAA ATC CTC GAT GTG AGT TTC TGC TTT GCT GTG TGG GGG TCC ATG GTA GGA C
EGFR Exon 19 wild-type 160 nt Synthetic DNA, reverse	GTC CTA CCA TGG ACC CCC ACA CAC CAA AGC AGA AAC TCA CAT CGA GGA TTT CCT TGT TGG CTT TCG GAG ATG TTG CTT CTC TTA ATT CTT TGA TAG CGA CGG GAA TTT TAA CTT TCT CAC CTT CTG GGA TCC AGA GTC CCT ATG ACA GAG AGA GAA GGA A
Tile 1 binding to forward strands of Exon 19 deletion mutations and wild-type DNAs, 16 nt	CAGAGAGAGAAGGAAG
Tile 2 binding to forward strands of Exon 19 deletion mutations (COSM 6223 and 6225), 14 nt	ATCCAGAGTCCCTA
Tile 3 binding to forward strands of Exon 19 deletion mutations (COSM 6223 and 6225), 16 nt	TTAACTTTCTCACCTT
Tile 4 binding to forward strands of Exon 19 deletion mutations (COSM 6223 and 6225), 14 nt	TCACATCGAGGATT
Tile 5 binding to forward strands of Exon 19 deletion mutations (COSM 6223 and 6225), 18 nt	CCCCCACACACCAAAGCA
Tile 6 binding to forward strands of Exon 19 deletion mutations (COSM 6223 and 6225), 13 nt	GTTCAGAGCCATG

Auxiliary Probe binding to the forward strands of EGFR exon 19 deletion mutations and wild-type DNAs, 24 nt	CTTGTTGGCTTTCACACATAGTCT
LNA Capture Probe Blocker, 11 nt	TTCCCGTCGCT
Cy5 Fluorescent Probe, 8 nt, for Exon 19 Deletion Mutation, COSM 6223	/Cy5/ATGTTTTG
Cy5 Fluorescent Probe, 8 nt, for Exon 19 Deletion Mutation, COSM 6225	/Cy5/ATGTCTTG
Cy3 Fluorescent Probe, 9 nt	AGACTATGT/Cy3/